Chinese Chemical Letters 37 (2026) 111603

Contents lists available at ScienceDirect

Chinese Chemical Letters

journal homepage: www.elsevier.com/locate/cclet

Facile ammonium salt-mediated double-deck stacking strategy of Li_3YCl_6 halide solid electrolytes for all-solid-state lithium-metal batteries

Cheng-Jin Liu, Jia-Xiang Wan, Chang Miao*, Zhi-Yan Wang, Wei Xiao*

College of Chemistry and Environmental Engineering, Yangtze University, Jingzhou 434023, China

ARTICLE INFO

Article history:
Received 8 June 2025
Revised 7 July 2025
Accepted 17 July 2025
Available online 17 July 2025

Keywords:
Halide solid electrolyte
Li_3YCl_6
Ammonium salt
Double-deck stacking strategy
All-solid-state lithium-metal battery

ABSTRACT

A facile ammonium salt-mediated double-deck stacking strategy is first put forward to fabricate Li_3YCl_6 (LYC) halide solid electrolyte (HSE), which capitalizes on the dual functionality of NH_4Cl in terms of dehydration and chlorination. It is worth mentioning that the obtained LYC features nanoparticles (<400 nm) and demonstrates an excellent ionic conductivity of 2.33×10^{-4} S/cm at 25 °C. In addition, the integration of LYC into all-solid-state cell with $LiCoO_2$ cathode and Li anode delivers a high initial discharge specific capacity of 139.5 mAh/g at 0.1 C with a capacity retention ratio of 87.7 % after 50 cycles. Encouragingly, the well-designed strategy not only enables the adoption of low-cost metal oxides and hydrates as raw materials, but also realizes the regeneration of damp LYC HSE. Hence, these encouraging results manifest that the proposed synthesis strategy delivers extremely economic benefits and valuable insights for developing HSEs.

© 2026 Published by Elsevier B.V. on behalf of Chinese Chemical Society and Institute of Materia Medica, Chinese Academy of Medical Sciences.

Lithium-ion batteries (LIBs) are regarded as highly promising energy storage devices [1–3], yet flammable organic liquid electrolytes in traditional LIBs easily trigger critical safety hazards including gas release, fire, and even explosion [4–7], which make LIBs tricky to satisfy the ever-growing demands for high energy density and excellent safety simultaneously. Hence, all-solid-state lithium-metal batteries (ASSLMBs), which employ Li anode and non-flammable inorganic solid electrolytes (ISEs), have been developed to grapple with above dilemmas of traditional LIBs [8–10]. Moreover, ASSLMBs demonstrate significantly enhanced energy density and safety to possess immense application potentials, in which ISEs served as pivotal components have been extensively explored for decades and play a vital role in cycling stability, rate performance, and longevity of ASSLMBs [11–13]. Among numerous candidates, oxides and sulfides are considered as potential candidate materials over the last decade. Despite wide electrochemical working window [14–16], inherent mechanical rigidity and brittleness of oxides are stumbling blocks for ASSLMBs assembly and electrolyte-cathode intimate interfacial contact [17–19], which hinder Li^+ ions transport and increase impedance to some extent. By contrast, sulfides not only demonstrate ductile nature allowing simple cold pressing and perfect solid-solid contact [20,21], but also deliver ultra-high ionic conductivity comparable to organic liquid electrolytes [22,23]. Nevertheless, the exposure of sulfides to moist air easily leads to the release of toxic H_2S gas, ineluctably posing a threat to both human health and environment [24,25]. Moreover, the intrinsically inferior electrochemical stability limits direct contact between sulfides and typical high-voltage cathodes in the absence of appropriate protective layers [26,27], which gives rise to a series of extra challenges subsuming the identification of suitable coating materials and the fabrication of uniform functional coating layers coupled with appropriate thickness. In consequence, it is necessary to exploit ISEs materials with excellent ionic conductivity, high oxidative stability, and satisfactory mechanical property simultaneously.

Fortunately, Li-M-X (M = metal; X = F, Cl, Br, and I) halide solid electrolytes (HSEs) meet aforementioned requirements and have captured considerable research interests lately [28–30]. As a matter of fact, the origin of HSEs can be traced back to the investigation of LiI conductor as early as the 1930s [31,32]. In this regard, HSEs are equivalent to substituting of Li^+ ions by other metal ions on the basis of LiX (X = F, Cl, Br, and I), which can facilitate ionic conduction by inducing local disordered sublattice and structural distortion as well as enriching lithium vacancy [33–35]. Regrettably, early-stage HSEs synthesized *via* prolonged solid-state reactions fail to attract tremendous attention owing to the quite low room-temperature ionic conductivity of about 10^{-7} S/cm

* Corresponding authors.
E-mail addresses: miaochang2004@163.com (C. Miao), xwylyq2006@126.com (W. Xiao).

https://doi.org/10.1016/j.cclet.2025.111603
1001-8417/© 2026 Published by Elsevier B.V. on behalf of Chinese Chemical Society and Institute of Materia Medica, Chinese Academy of Medical Sciences.

[36–38]. Encouragingly, the emergence of Li_3YCl_6 (LYC) synthesized by high-energy ball milling greatly boosts the development of HSEs due to the high ionic conductivity, deformability, and electrochemical stability [39]. However, expensive anhydrous halide raw materials are required for preparing HSEs by mechanochemical ball milling synthesis strategy, which necessitate strict inert atmosphere or vacuum due to the extreme moisture sensitivity, thus increasing the preparation cost and operation difficulty. Notably, the low-density raw materials firmly adhere to both grinding ball surface and jar wall during high-energy ball milling, causing raised handling challenges and unnecessary product loss during iterative scraping and grinding processes [40,41]. Even so, the widely used synthesis methods remain conventional solid-state reaction and mechanochemical milling approaches. For instance, Yang *et al.* [42] have fabricated LYC by manual grinding raw materials and annealing at 450 °C for 24 h, while the ionic conductivity of LYC is merely 2.0×10^{-5} S/cm. Analogously, Ito *et al.* [43] have synthesized LYC with the ionic conductivity of 1.2×10^{-4} S/cm by annealing at 322 °C for 50 h. In contrast, LYC prepared by ball milling at 500 rpm for 52 h exhibits a relatively higher ionic conductivity of 2.24×10^{-4} S/cm [44]. It is worth noting that above synthesis protocols exclusively employed anhydrous LiCl and YCl_3 to eliminate moisture interference. Apparently, the ionic conductivity of HSEs shows strong process-dependence, even with order-of-magnitude variations observed across different synthesis routes. Consequently, the pursuit of high ionic conductivity at the same time as economical production and simple processing is still a major challenge for the preparation of HSEs.

Hence, the ammonium salt-mediated double-deck stacking strategy is proposed to cut the cost and streamline the process, in which the thermal decomposition products and the dehydration effect of NH_4Cl contribute to optimizing synthesis atmosphere and yielding high-purity HSEs. In this work, the effects of annealing temperature on crystal structure, micromorphology, and intrinsic property of obtained LYC are systematically explored. Moreover, LYC exhibits excellent ionic conductivity and electrochemical stability window, and the assembled all-solid-state cells demonstrate outstanding cycling stability. Inspiringly, the proposed strategy can not only adopt inexpensive metal oxides and hydrates as raw materials to be blessed with higher economic profit, but also afford to fabricate $LiYF_4$ and Li_3FeCl_6 successfully to demonstrate the potential scalability. Thus, the handy synthesis strategy may offer a new idea for realizing economical commercial production and application of Li-M-X-typed HSEs.

An ammonium salt-mediated double-deck stacking synthesis strategy is first proposed to prepare LYC, and the specific schematic diagram is displayed in Fig. 1a. Noticeably, NH_4Cl in the mixed layer removes the coordinated water of $YCl_3{\cdot}6H_2O$ under 200 °C to form an intermediate product $(NH_4)_3YCl_6$ (Fig. S1 in Supporting information), which subsequently reacts with LiCl to generate targeted LYC in the following annealing process. The excessive part of NH_4Cl in the mixed layer aims at converting YOCl byproduct to YCl_3. Moreover, HCl and NH_3 generated from the decomposition of bottom-layer NH_4Cl contribute to establishing a more favorable preparation atmosphere, in which ascending HCl gas can sufficiently react with possible impurity Y_2O_3 to form YCl_3. The conversion of YOCl and Y_2O_3 byproducts can ensure the high purity of obtained LYC. The possible involved main chemical reactions during the whole process are listed in the following Eqs. 1–5.

$$YCl_3{\cdot}6H_2O + 3NH_4Cl \rightarrow (NH_4)_3YCl_6 + 6H_2O \quad (1)$$

$$(NH_4)_3YCl_6 + 3LiCl \rightarrow Li_3YCl_6 + 3NH_3 + 3HCl \quad (2)$$

$$YOCl + 2NH_4Cl \rightarrow YCl_3 + 2NH_3 + H_2O \quad (3)$$

$$Y_2O_3 + 6HCl \rightarrow 2YCl_3 + 3H_2O \quad (4)$$

$$YCl_3 + 3LiCl \rightarrow Li_3YCl_6 \quad (5)$$

To explore the effect of annealing temperature on the structure and composition of LYC and to ascertain the optimal annealing temperature, XRD patterns of LYC powders synthesized under

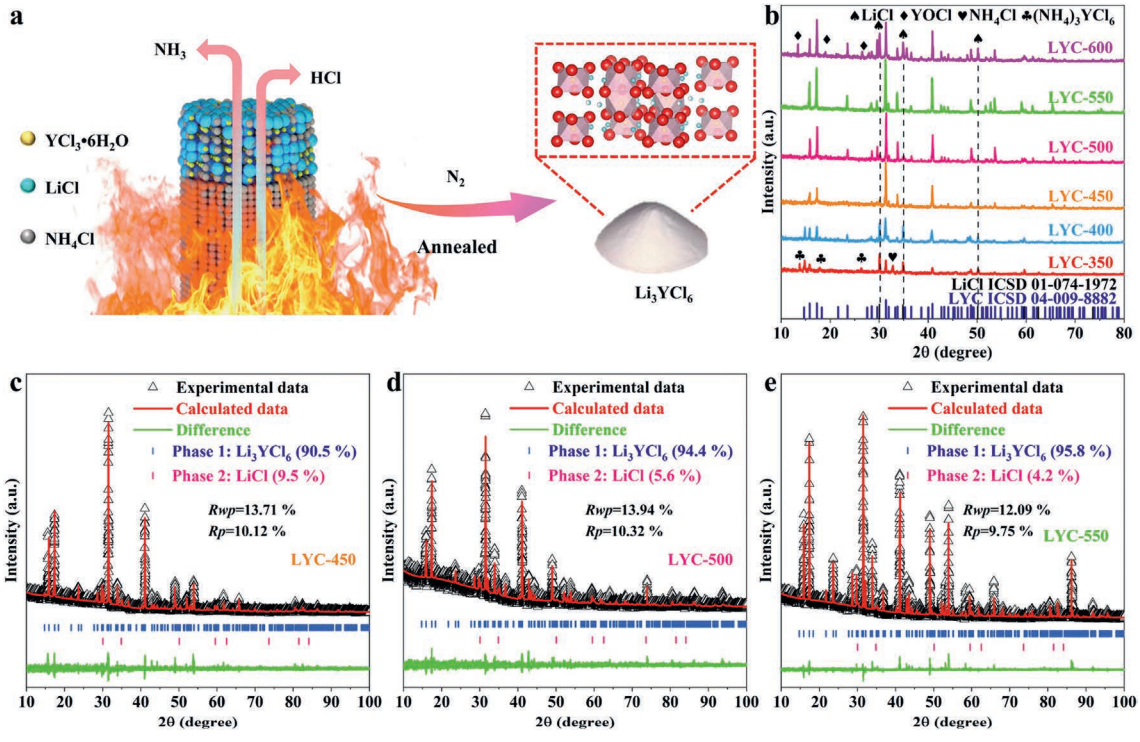


Fig. 1. (a) Schematic illustration of the fabrication process for LYC. (b) XRD patterns of as-prepared samples. Refinement profiles of (c) LYC-450, (d) LYC-500, and (e) LYC-550.

various annealing temperatures are demonstrated in Fig. 1b. Characteristic peaks of LiCl, $(NH_4)_3YCl_6$, and NH_4Cl in LYC-350 indicate such a low annealing temperature is insufficient for the complete decomposition of $(NH_4)_3YCl_6$ and excess NH_4Cl, as further confirmed by the existence of N element in Fig. S2 (Supporting information). When the annealing temperature reaches 400 °C, XRD signals of LYC-400 are well matched with *P*-3*m*1 and *Fm*-3*m* space groups, manifesting successful formation of LYC but also the presence of substantial unreacted LiCl. Upon increasing the annealing temperature to 450–550 °C, LiCl-related XRD peak intensity is significantly reduced, demonstrating more adequate reactions between LiCl and $(NH_4)_3YCl_6$. Additionally, LYC-450, LYC-500, and LYC-550 are predominantly crystallized in trigonal LYC phase with a small amount in LiCl phase, and the crystallinity is obviously improved with increasing annealing temperature. Nevertheless, too high crystallinity may be detrimental to ionic conductivity [39]. With further improving annealing temperature to 600 °C, evident YOCl and LiCl impurities can be detected in LYC-600. Accordingly, LYC-450, LYC-500, and LYC-550 as main research objects are taken into consideration for the following investigations. Since the extremely low ionic conductivity of LiCl ($\sim 10^{-11}$ S/cm) may worsen the ionic conductivity, the relative content of LiCl and LYC in LYC-450, LYC-500, and LYC-550 is determined by refining the XRD patterns. It can be observed from Figs. 1c-e that the relative content of LiCl monotonically decreases from 9.5 % to 4.2 % with enhanced annealing temperature. According to the above results, it is reasonable to speculate that LYC-500 possesses superior ionic conductivity among these samples.

To further analyze chemical composition of LYC-500, high-resolution XPS spectra of Li 1s, Y 3d, and Cl 2p are captured and displayed in Figs. 2a-c. Evidently, the peak at 56.6 eV in Li 1s spectra can be assigned to single valence Li^+ originated from LiCl and LYC. Additionally, characteristic peaks of Y $3d_{3/2}$ and Y $3d_{5/2}$ at 161.1 and 158.9 eV in Y 3d spectra are associated with Y^{3+}, and Cl $2p_{1/2}$ and Cl $2p_{3/2}$ peaks at 200.5 and 198.8 eV in Cl 2p spectra can be assigned to Cl^-. The above conclusions prove the successful synthesis of LYC without other oxides or oxychlorides according to the designed strategy, which are in well accord with the XRD results. Moreover, Fig. 2d and Fig. S3 (Supporting information) demonstrate uniformly distributed Y and Cl elements in the LYC HSE. Even though the particle size enlarges slightly with increasing annealing temperature, as-synthesized LYC-450, LYC-500, and LYC-550 maintain nanoscale stone-like morphology with particle sizes below 400 nm. The nanoscale particle size plays a positive role in achieving more efficient and intimate contact with other components inside the battery. Additionally, nanoscale particles are conductive to enhancing compactness under cold pressing, which is reflected in the dense LYC-500 pellet in Fig. 2e. It can be found from TEM (Fig. S4 in Supporting information) and HR-TEM (Fig. 2f) images that plentiful lattice defects such as dislocations and distortions are distinctly detected in LYC-500. These defects contribute to facilitating Li^+ ions conduction by expanding the migration channels of Li^+ ions and enriching concentration of charge carriers.

The electrochemical impedance spectra (Figs. 3a-c) at the temperature gradient from 25 °C to 85 °C are determined by AC impedance measurement of stainless steel (SS) symmetric cells based on LYC-450, LYC-500, and LYC-550, which consist of a semicircle at high frequency range and an oblique line at low frequency range. The corresponding Arrhenius profiles according to Nyquist plots are illustrated in Fig. 3d in the form of $\ln(\sigma T)$ *vs.* $1000/T$, in which σ and T represent ionic conductivity and Kelvin temperature. Meanwhile, the perfect linear relationship between $\ln(\sigma T)$ and $1000/T$ manifests the reliability of calculated results. The calculated ionic conductivity at 25 °C and activation energy of LYC-450, LYC-500, and LYC-550 are summarized in Fig. 3e. Specifically, LYC-500 delivers the highest ionic conductivity of 2.33×10^{-4} S/cm at 25 °C with the lowest activation energy of 0.365 eV compared with LYC-450 (1.13×10^{-4} S/cm, 0.410 eV) and LYC-550 (1.28×10^{-4} S/cm, 0.403 eV), which are well consistent with the above-mentioned speculations about XRD results. The highest ionic conductivity of LYC-500 can be interpreted as relatively low content of LiCl impurity and appropriate crystallinity. Specifically, appropriate crystallinity of LYC can weaken the Li^+-blocking barrier induced by the repulsive interaction between Y^{3+} and Li^+ ions [39,43]. Moreover, electronic conductivities of LYC-450, LYC-500, and LYC-550 are calculated from steady-state current values of related symmetric cells displayed in Fig. 3f, in which LYC-500 exhibits the lowest electronic conductivity of 1.04×10^{-9} S/cm, implying that the lithium dendrite growth inside LYC-500 pellet can be effectively restrained during the cycling process. Noteworthily, the electronic conductivity of LYC-500 is five orders of magnitude lower than the ionic conductivity. Such a huge

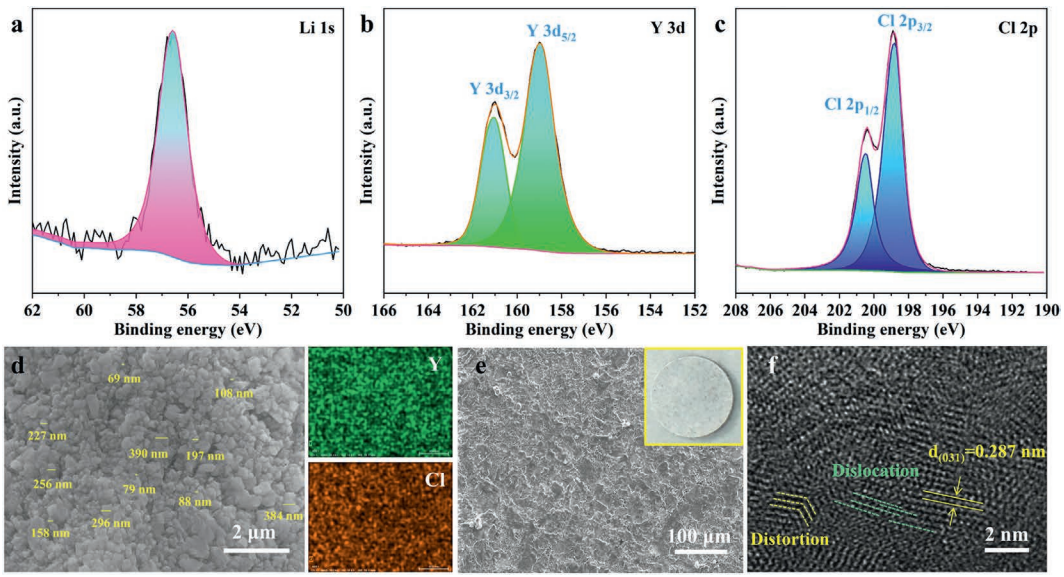


Fig. 2. XPS spectra of (a) Li 1s, (b) Y 3d, and (c) Cl 2p along with (d) FE-SEM and EDS images of LYC-500. (e) Digital photo and related FE-SEM image of LYC-500 pellet under 400 MPa. (f) HR-TEM image of LYC-500.

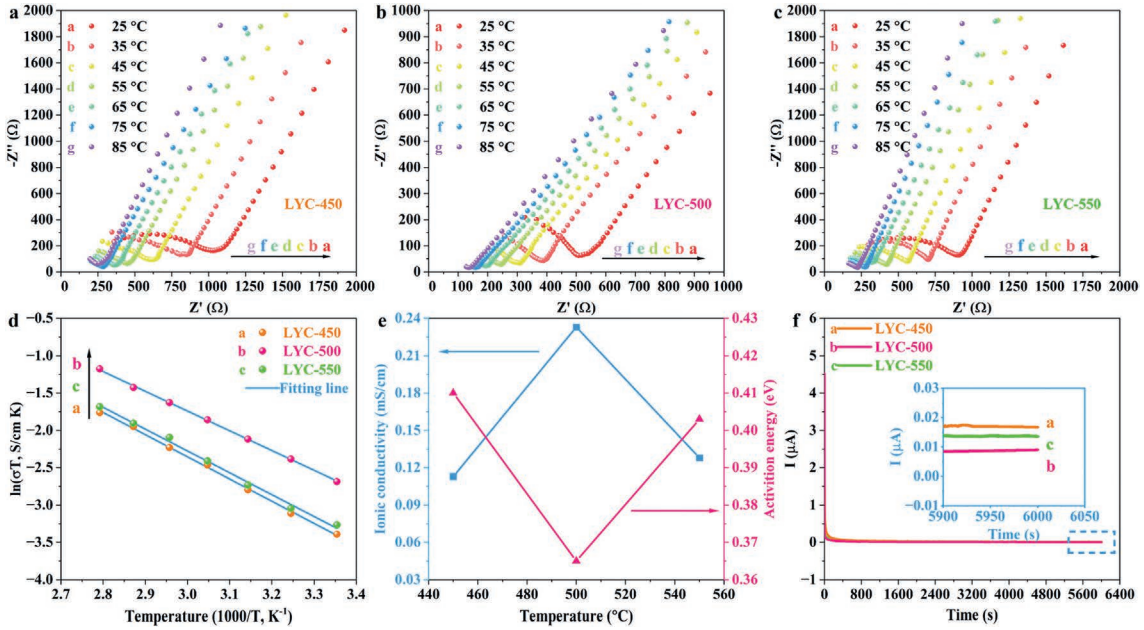


Fig. 3. (a-c) Nyquist plots at different temperatures and (d) corresponding Arrhenius plots of SS/LYC-450/SS, SS/LYC-500/SS, and SS/LYC-550/SS cells. (e) Ionic conductivity at 25 °C and activation energy of LYC-450, LYC-500, and LYC-550. (f) DC polarization curves of SS/LYC-450/SS, SS/LYC-500/SS, and SS/LYC-550/SS cells.

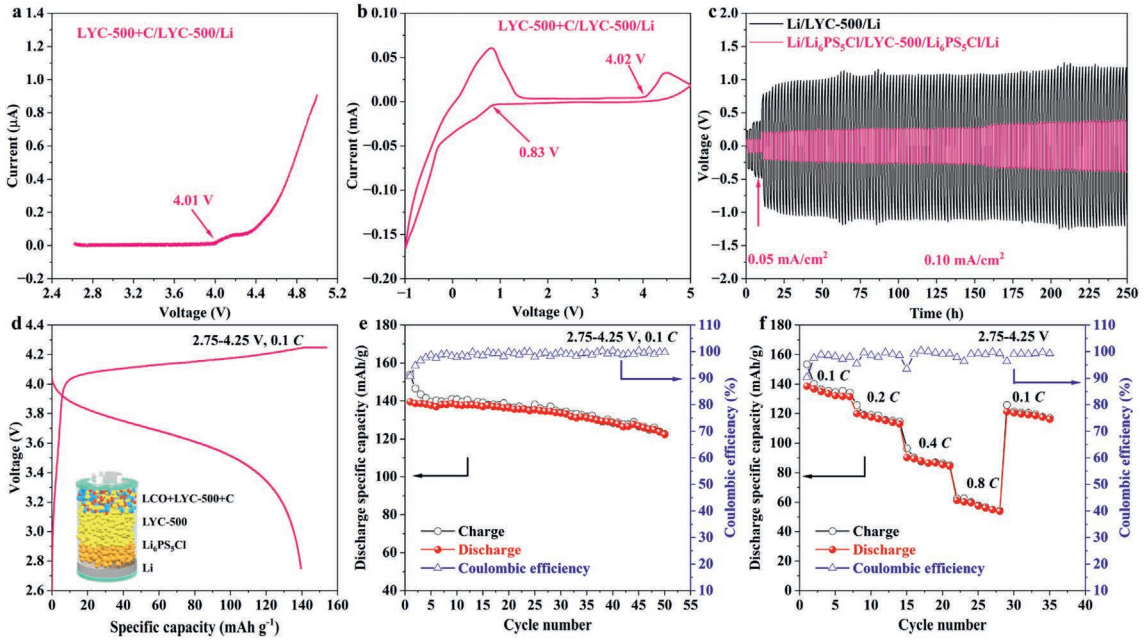


Fig. 4. (a) LSV and (b) CV profiles of LYC-500 + C/LYC-500/Li cell. (c) Galvanostatic cycling profiles of Li/LYC-500/Li and Li/Li_6PS_5Cl/LYC-500/Li_6PS_5Cl/Li symmetric cells. (d) Initial charge/discharge, (e) cycle, and (f) rate curves of LCO+LYC-500 + C/LYC-500/Li_6PS_5Cl/Li.

distinction between electronic conductivity and ionic conductivity demonstrates prominent application potential of LYC-500 as a promising solid electrolyte with ultra-low electronic conductivity and excellent ionic conductivity in terms of ASSLMBs.

In addition to high ionic conductivity and low electronic conductivity, interface compatibility of HSEs toward both cathode and anode is also critical for the cycling stability of ASSLMBs. As a consequence, LSV and CV measurements are carried out on LYC-500 + C/LYC-500/Li cell to evaluate the electrochemical stability of LYC-500. Notably, the LYC-500 + C/LYC-500/Li cell displays a high oxidation potential at about 4.01 V related to the oxidation process of Cl^- *via* LSV analysis in Fig. 4a, demonstrating that LYC-500 can be compatible with high-voltage oxide cathode materials without extra protective coating. Analogously, CV profiles (Fig. 4b) of LYC-500 + C/LYC-500/Li cell exhibit an oxidation potential similar to the LSV results. Unfavorably, the cell delivers an anodic current response at around 0.83 V, indicating that LYC-500 is unstable against Li metal anode. Hence, Li_6PS_5Cl as an insulating layer is inserted between LYC-500 pellet and Li anode to impede electron transport across the LYC-500/Li interface and stabilize the interface. To verify the feasibility of Li_6PS_5Cl interlayer, the interface compatibility toward Li metal is investigated from Li/LYC-500/Li and Li/Li_6PS_5Cl/LYC-500/Li_6PS_5Cl/Li symmetric cells by galvanostatic lithium stripping and plating. Encouragingly, a lower overpotential of about 0.37 V is detected for Li/Li_6PS_5Cl/LYC-500/Li_6PS_5Cl/Li than that of about 1.18 V for Li/LYC-500/Li after be-

ing cycled for 250 h (Fig. 4c), testifying Li_6PS_5Cl interlayer effectively stabilizes the LYC-500/Li interface.

To assess the electrochemical performance of all-solid-state cells employing LYC-500, the cells with a configuration of LCO + LYC-500 + C/LYC-500/Li_6PS_5Cl/Li are assembled, in which the introduction of Li_6PS_5Cl layer aims at preventing LYC-500 from being reduced by Li anode, and the corresponding electrochemical performance curves are displayed in Figs. 4d-f. It can be clearly detected from Fig. 4d that the assembled cell delivers an initial discharge specific capacity of 139.5 mAh/g at 0.1 C with an initial coulombic efficiency of 90.7 %. Impressively, the cell remains an excellent capacity retention ratio of 87.7 % with an average coulombic efficiency of 98.8 % over 50 cycles (Fig. 4e). Moreover, the rate capability of the LYC-500-based cell is displayed in Fig. 4f, in which the average discharge specific capacity at 0.1, 0.2, 0.4, and 0.8 C is 134.1, 116.4, 87.3, and 57.6 mAh/g, respectively. It is worth mentioning that the average discharge specific capacity of the LCO + LYC-500 + C/LYC-500/Li_6PS_5Cl/Li cell can recover to 119.0 mAh/g at 0.1 C after undergoing a series of gradient current densities. The excellent electrochemical performance of the LCO + LYC-500 + C/LYC-500/Li_6PS_5Cl/Li cell benefits from the dense structure and high-efficiency ionic conduction of LYC-500, which are inseparable from good ductility and nanoscale particle size of LYC-500 synthesized by the double-deck stacking synthesis strategy.

Given the extreme challenge in storing and transporting water-sensitive HSEs, the damp LYC-500 is further reprocessed *via* our ammonium salt-mediated double-deck stacking synthesis strategy to assess whether the strategy enables the reuse of disabled LYC HSEs. The resulting powders are designated as LYC-reannealed, which still maintains the trigonal *P*-3*m*1 phase structure (Fig. S5 in Supporting information), certifying the proposed synthesis strategy can indeed realize the recovery of hygroscopic LYC-500. Specifically, $LiCl{\cdot}H_2O$ and $YCl_3{\cdot}6H_2O$ hydrolysis products [45] derived from LYC after humidity exposure can be used as reactants for the synthesis strategy by dehydration effect of NH_4Cl to regenerate LYC. In addition, LYC-reannealed sample delivers similar nanoparticle morphology to LYC-500 (Fig. S6 in Supporting information), but moderately reduced ionic conductivity of 1.13×10^{-4} S/cm at 25 °C (Fig. S7a in Supporting information) and elevated activation energy of 0.383 eV (Fig. S7b in Supporting information). Although the ionic conductivity and activation energy of LYC-reannealed are slightly inferior to those of fresh LYC-500, both parameters remain within the acceptable range, manifesting the efficacy of this strategy for realizing the reuse of exposed LYC. Impressively, LYC-Y_2O_3 synthesized by Y_2O_3 as Y source exhibits the same crystal structure as LYC-500 (Fig. S8a in Supporting information) and delivers an excellent ionic conductivity of 1.55×10^{-4} S/cm (Fig. S8b in Supporting information). Notably, Y_2O_3 (51.1 USD/kg) and $YCl_3{\cdot}6H_2O$ (38.4 USD/kg) demonstrate significantly lower costs than anhydrous YCl_3 (704.2 USD/kg), achieving ~90 % reduction in raw material costs (All unit prices of each raw material with 99.99 % purity originate from MACKLIN). More importantly, the synthesis strategy may be capable of synthesizing multiple Li-M-X HSEs. For instance, $LiYF_4$ synthesized from LiF, YF_3, and NH_4F exhibits an ionic conductivity of 9.35×10^{-5} S/cm (Fig. S9 in Supporting information), while Li_3FeCl_6 prepared from LiCl, $FeCl_3{\cdot}6H_2O$, and NH_4Cl displays an ionic conductivity of 1.06×10^{-4} S/cm (Fig. S10 in Supporting information). Accordingly, the well-designed synthesis strategy not only successfully achieves the regeneration of hygroscopic LYC but also generalizes to synthesize multiple Li-M-X HSEs.

Ammonium salt-mediated double-deck stacking strategy is first proposed to synthesize LYC by making the best of dehydration, thermal decomposition, and chlorination of NH_4Cl, which not only inhibits the hydrolysis of YCl_3, but also converts YOCl and Y_2O_3 to YCl_3 as well as constructing more favorable preparation atmosphere. The obtained LYC-500 is endowed with excellent ionic conductivity of 2.33×10^{-4} S/cm, low electronic conductivity of 1.04×10^{-9} S/cm, and ideal electrochemical stability window as high as 4.01 V. Precisely, the LCO + LYC-500 + C/LYC-500/Li_6PS_5Cl/Li cell delivers an initial discharge specific capacity of 139.5 mAh/g at 0.1 C and an excellent capacity retention ratio of 87.7 % after 50 cycles. Intriguingly, the hygroscopic LYC-500 reprocessed with the strategy presents slightly decreased ionic conductivity of 1.13×10^{-4} S/cm. Moreover, low-cost metal oxides and hydrated metal halides are permitted to serve as synthetic raw materials, thus expanding the selection of raw materials for HSEs synthesis and reducing the fabrication cost. Hence, the proposed strategy provides a new direction for the economical synthesis of Li-M-X HSEs with excellent properties.

CRediT authorship contribution statement

Cheng-Jin Liu: Writing – original draft, Methodology, Investigation, Data curation. **Jia-Xiang Wan:** Visualization, Formal analysis, Data curation. **Chang Miao:** Resources, Methodology, Funding acquisition. **Zhi-Yan Wang:** Methodology, Investigation, Conceptualization. **Wei Xiao:** Writing – review & editing, Supervision, Funding acquisition, Conceptualization.

Declaration of compeing interest

The authors declare that they have no known competing financial interests or personal relationships that could have appeared to influence the work reported in this paper.

Acknowledgments

This work was financially supported by the National Natural Science Foundation of China (No. 52274292), the Outstanding Youth Foundation of Hubei Province (No. 2020CFA090), the Natural Science Foundation of Hubei Province (No. 2025AFB376), and the Young Top-notch Talent Cultivation Program of Hubei Province.

Supplementary materials

Supplementary material associated with this article can be found, in the online version, at doi:10.1016/j.cclet.2025.111603.

References

[1] S.Q. Nie, W. Xiao, S. Pan, et al., Chem. Eng. J. 494 (2024) 152983.
[2] C.R. Zeng, R.X. Zheng, F.X. Fan, et al., Energy Storage Mater. 72 (2024) 103788.
[3] C.J. Liu, C. Miao, M.Y. He, et al., J. Power Sources 566 (2023) 232961.
[4] S.J. Wang, K. Liang, H.S. Zhao, et al., Energy Storage Mater. 63 (2023) 103027.
[5] C.J. Liu, C. Miao, Z.W. Li, et al., Chem. Eng. J. 491 (2024) 152078.
[6] D.B. Thornton, B.J.V. Davies, S.B. Scott, et al., Angew. Chem. Int. Ed. 63 (2024) e202315357.
[7] C.J. Liu, Z.C. Yi, J.X. Wan, et al., Chem. Eng. J. 503 (2025) 158633.
[8] Z.Y. Wang, L. Shen, S.G. Deng, P. Cui, X.Y. Yao, Adv. Mater. 33 (2021) 2100353.
[9] H. Yan, J.M. Yao, Z.R. Ye, et al., Chin. Chem. Lett. 36 (2025) 109568.
[10] X.M. Shi, Z.C. Zeng, M.Z. Sun, et al., Nano Lett. 21 (2021) 9325.
[11] J. Park, D. Han, H. Kwak, et al., Chem. Eng. J. 425 (2021) 130630.
[12] W. Xiao, Z.Y. Wang, Z.Y. Zhang, et al., J. Power Sources 382 (2018) 128–134.
[13] C.H. Wang, R.Z. Yu, H. Duan, et al., ACS Energy Lett. 7 (2021) 410–416.
[14] M. Sakakura, K. Mitsuishi, T. Okumura, N. Ishigaki, Y. Iriyama, ACS Appl. Mater. Interfaces 14 (2022) 48547.
[15] W. Xiao, J.Y. Wang, L.L. Fan, J.J. Zhang, X.F. Li, Energy Storage Mater. 19 (2019) 379–400.
[16] T. Thompson, S. Yu, L. Williams, et al., ACS Energy Lett. 2 (2017) 462–468.
[17] S. Zhao, J. Lu, B.F. Sheng, et al., Chin. Chem. Lett. 36 (2025) 110008.
[18] F.Z. Zhang, Q.A. Huang, Z.P. Tang, et al., Nano Energy 70 (2020) 104545.
[19] K.J. Kim, M. Balaish, M. Wadaguchi, L.P. Kong, J.L.M. Pupp, Adv. Energy Mater. 11 (2020) 2002689.
[20] Z. Wu, X.H. Li, C. Zheng, et al., Electrochem. Energy R. 6 (2023) 10.
[21] Y. Kato, S. Hori, T. Saito, et al., Nat. Energy 1 (2016) 1–7.
[22] J.H. Wu, S.F. Liu, F.D. Han, X.Y. Yao, C.S. Wang, Adv. Mater. 33 (2021) 2000751.
[23] Z. Jiang, H.L. Peng, Y. Liu, et al., Adv. Energy Mater. 11 (2021) 2101521.
[24] K.H. Park, Q. Bai, D.H. Kim, et al., Adv. Energy Mater. 8 (2018) 1800035.
[25] J. Lee, T. Lee, K. Char, K.J. Kim, J.W. Jang, Acc. Chem. Res. 54 (2021) 3390–3402.

[26] C.H. Wang, X. Li, Y. Zhao, et al., Small Methods 3 (2019) 1900261.
[27] L.D. Zhou, N. Minafra, W.G. Zeier, L.F. Linda, Acc. Chem. Res. 54 (2021) 2717–2728.
[28] K. Wang, Z.Q. Gu, Z.W. Xi, L. Hu, C. Ma, Nat. Commun. 14 (2023) 1396.
[29] X.N. Li, J.W. Liang, X.F. Yang, et al., Energy Environ. Sci. 13 (2020) 1429–1461.
[30] X.N. Li, J.W. Liang, J.T. Kim, et al., Adv. Mater. 34 (2022) 2200856.
[31] B.J.H. Jackson, D.A. Young, J. Phys. Chem. Solids 30 (1969) 1973–1976.
[32] T.E. Phipps, W.D. Lansing, T.G. Cooke, J. Am. Chem. Soc. 48 (2002) 112–125.
[33] L.J. Huang, L. Zhang, J.Y. Bi, et al., Energy Mater. Adv. 4 (2024) 0092.
[34] H.D. Lutz, W. Schmidt, H. Haeuseler, J. Phys. Chem. Solids 42 (1981) 287–289.
[35] J.W. Liang, X.N. Li, K.R. Adair, X.L. Sun, Acc. Chem. Res. 54 (2021) 1023–1033.
[36] K. Yamada, K. Kumano, T. Okuda, Solid State Ionics 177 (2006) 1691–1695.
[37] K. Yamada, K. Kumano, T. Okuda, Solid State Ionics 179 (2008) 867–870.
[38] Y. Zhao, L.L. Daemen, J. Am. Chem. Soc. 134 (2012) 15042–15047.
[39] T. Asano, A. Sakai, S. Ouchi, et al., Adv. Mater. 30 (2018) e1803075.
[40] R. Schlem, S. Muy, N. Prinz, et al., Adv. Energy Mater. 11 (2021) 2101022.
[41] L.P. Wang, J.H. Han, F.J. Ma, X.K. Li, D. Wang, J. Clean. Prod. 406 (2023) 137100.
[42] S. Yang, S.Y. Kim, G. Chen, ACS Energy Lett. 9 (2024) 2212–2221.
[43] H. Ito, Y. Nakahira, N. Ishimatsu, et al., B. Chem. Soc. Jpn. 96 (2023) 1262.
[44] M. Yamagishi, C. Zhong, D. Shibata, M. Morimoto, Y. Orikasa, Electrochemistry 91 (2023) 037002.
[45] X.N. Li, J.W. Liang, K.R. Adair, et al., Nano Lett. 20 (2020) 4384–4392.